S.1 Chemical Mass Balance model

Chemical mass balance (CMB) models are typically used as receptor models for cases where source profiles are known, and only the mass loading information needs resolving (Friedlander, 1973; Gordon, 1988;Hopke, 1991a; Miller et al., 1972). In receptor modelling based on mass conservation, the observed loading x of variable v at sampling time t can be modelled as a sum of contributions from all sources $s = 1…p$ (e.g. Hopke, 1991b):

$$x_{v,t} = \sum_{s=1}^{p} f_{v,s} m_{s,t} + \varepsilon_{v,t}. \tag{S.1}$$

The contribution from a single source $(f_{v,s} m_{s,t})$ is the total mass, $m_{s,t}$, emitted from that source multiplied by the fraction of variable v in the emission profile of said source, $f_{v,s}$. The residual $\varepsilon_{v,t}$ encompasses the difference between observation and the model.

S.2 Mass scaling optimisation
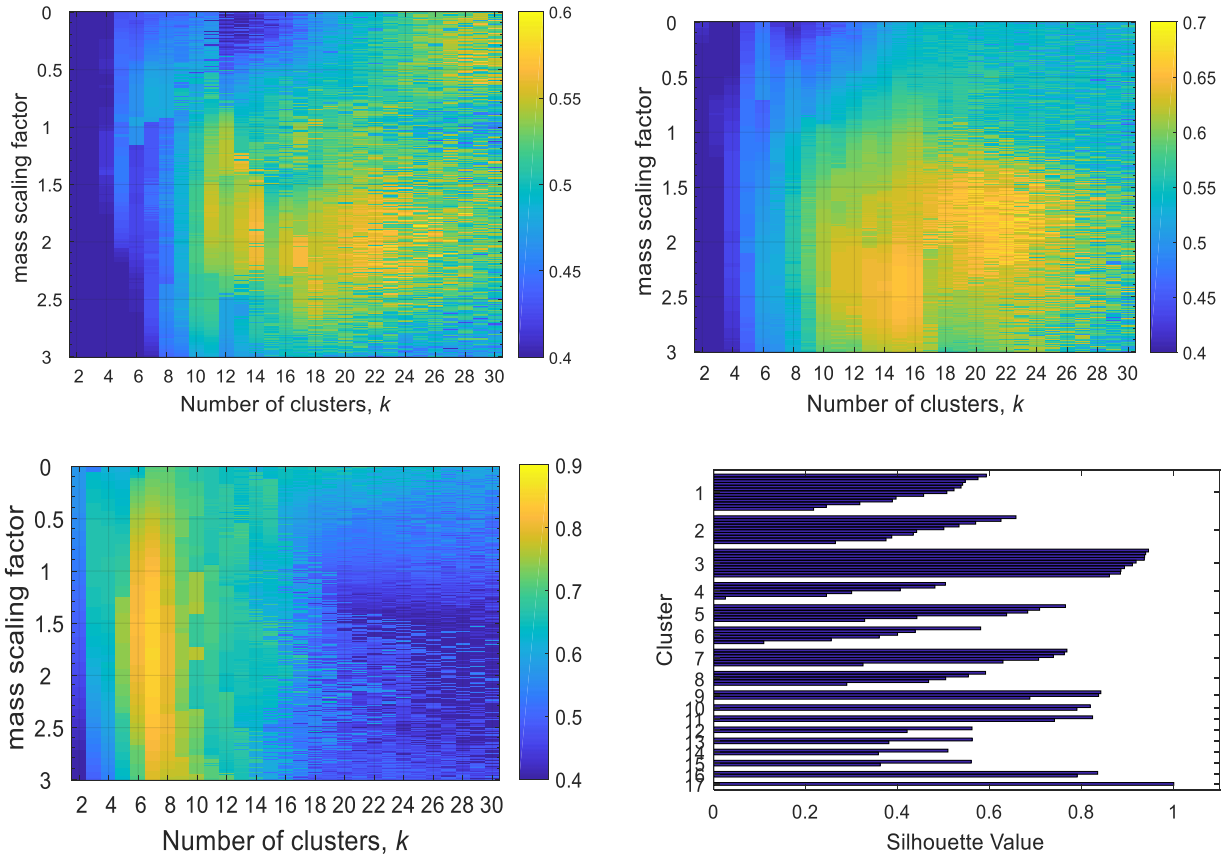
Figure S.1. Clustering silhouette scans for phases I (upper left), II (upper right) and III (lower left) panels. x-axis comprises cluster number (k) and y-axis the mass scaling factor s_m (Equation 4). Brighter colour (higher silhouette) indicates better solution quality. Note the different colour scales in panels. Stable silhouette maxima (i.e. not sensitive to minor, 0.01 changes in s_m) solutions were preferred. The solutions we selected were for P-I: k=17, s_m=2.12, for P-II: k=15, s_m=2.41 and for P-III: k=7, s_m=1.81). In lower right
5 **panel: object specific silhouettes (s_i) by cluster for the selected P-I solution.**

Beside the selected solutions described in Sections 3.1.1 to 3.1.3, there are other solutions of mathematically (near) equal quality available, resulting in slightly different classifications. When deciding on clustering solutions, we also explored the highest, alternative local maxima. While a comprehensive description of the clustering solution space is out of the scope of what we can present here, we note the main differences between the solutions relate to outlier groups and how they can be

10 combined or separated from the main classes. In phase I, the other viable solution would have been the maxima at k = 14 (s_m = 1.88 gives approximately the same classification as the selected solution at k = 17 (s_m = 2.12). We selected the latter solution since it yields a higher silhouette a) overall (0.5645 vs 0.5628) and b) for the AN cluster specifically (0.48 vs 0.35).

For both P-I and P-II, there exist a number of unstable (in relation to minor s_m change), high k solutions. However, upon inspection, their high silhouettes (compared to lower k solutions) seem to result from division of outlier clusters (n = 2…3,

15 with low within-cluster silhouettes), into singleton (n = 1) clusters. We find that including solutions with such further divisions does not incorporate new information, but rather smears the picture when aiming to interpret the outlier clusters (Section 3.4).

S.3 Ion pairing scheme

In the pairing schemes of Gysel et al. (2007) and Hong et al. (2017), nitrate, sulphate or ammonium are not allowed to exist separately from inorganic salts (e.g. organonitrate, organic sulphate or organic acid salt with ammonium). Since there is

20 evidence of especially organonitrates representing a considerable fraction of total particulate nitrate (e.g. Kiendler-Scharr et al., 2016), we modify the Hong et al. scheme to allow organic nitrate and "excess" ammonium (i.e. NH_4 existing with other species, such as organics). Organic sulphate was not included since it is not possible to differentiate between the two possible forms of "excess sulphur" (from the perspective of inorganic salt balance): sulphuric acid and organosulphate. To maintain compatibility with previous schemes, a sulphuric acid class was included. Any potential organosulphates would also fall into

25 the sulphuric acid class.

Our ion balance scheme, modified from Hong et al., (2017), is divided into three cases:

Case 1: Aerosol is acidic, not enough [NH_4^+] to convert all sulphate to NH_4HSO_4. Sulphate exists as sulphuric acid and ammonium bisulphate. All nitrate is organic, as sulphate formation is assumed preferential. All [NH_4^+] goes to ammonium

30 bisulphate.

$$\frac{[NH_4^+]}{[SO_4^{2-}]} < 1$$

sulphuric acid: $[H_2SO_4] = [SO_4^{2-}] - [NH_4^+]$ (S.2)

ammonium bisulphate: $[NH_4HSO_4] = [NH_4^+]$

ammonium sulphate: $[(NH_2)SO_4] = 0$

ammonium nitrate: $[NH_4NO_3] = 0$

organonitrate: $[org\ NO_3] = [NO_3^-]$

excess ammonium: $[excess\ NH_4] = 0$

Case 2: Aerosol is partly neutralised, sulphate exists as ammonium bisulphate and ammonium sulphate. Any nitrate is organic. All of $[NH_4^+]$ associates with sulphate.

$$1 \leq \frac{[NH_4^+]}{[SO_4^{2-}]} < 2$$

sulphuric acid: $[H_2SO_4] = 0$ $\hspace{3cm}$ (S.3)

10 ammonium bisulphate: $[NH_4HSO_4] = \left(2 - \frac{[NH_4^+]}{[SO_4^{2-}]}\right) * [SO_4^{2-}]$

ammonium sulphate: $[(NH_4)SO_4] = (\frac{[NH_4^+]}{[SO_4^{2-}]} - 1) * [SO_4^{2-}]$

ammonium nitrate: $[NH_4NO_3] = 0$

organonitrate: $[org\ NO_3] = [NO_3^-]$

excess ammonium: $[excess\ NH_4] = 0$

15

Case 3: Aerosol is fully neutralised, sulphate exists as ammonium sulphate. Leftover $[NH_4^+]$ from sulphate neutralisation goes with $[NO_3^-]$. In case all of $[NO_3^-]$ can be neutralised by $[NH_4^+]$, leftover $[NH_4^+]$ is labelled "excess NH_4^+", and assumed to bind with other species (e.g. organic acids).

$$2 < \frac{[NH_4^+]}{[SO_4^{2-}]}$$

20 sulphuric acid: $[H_2SO_4] = 0$ $\hspace{3cm}$ (S.4)

ammonium bisulphate: $[NH_4HSO_4] = 0$

ammonium sulphate: $[(NH_2)SO_4] = [SO_4^{2-}]$

ammonium nitrate: $[NH_4NO_3] = max([NO_3^-], [NH_4^+] - 2 * [SO_4^{2-}])$

organonitrate: $[org\ NO_3] = [NO_3^-] - [NH_4NO_3]$

25 excess ammonium: $[excess\ NH_4] = min(0, [NH_4^+] - 2 * [SO_4^{2-}] - [NO_3^-])$

We echo Hong et al. (2017) in emphasising that this approximation is only a first estimate of the dynamics of inorganic salt formation; the assumption of perfect internal mixing is likely unrealistic for atmospheric aerosol particles, due to the nature of atmospheric processing often affecting the particle outer surface, resulting in layered structures (e.g. Buajarern et al., 2007).

30 The model also does not adequately describe the thermodynamic equilibriums of salt formation or model the competition between $[SO_4^{2-}]$ and $[NO_3^-]$ for $[NH_4^+]$ realistically.

S.4 Relative ionisation efficiencies (RIEs) and ion pairing scheme sensitivity to RIE$_{NH4}$ changes

To convert from nitrate equivalent mass units (used in factorisation steps until P-III), the factorisation output data needs to be corrected for species-specific Relative Ionisation Efficiency (RIE; Allan et al., 2003; Jimenez et al., 2003). We thus summed the signals from individual ion species, and corrected them for RIE. Due to high uncertainties (standard deviation 51% of mean RIE) and for some data sets unavailability of relative ionisation efficiency calibrations for NH$_4$, we generally did not apply RIE correction for data sets individually, but instead used the default value of RIE$_{NH4}$ of 4.0 for AMS instruments. Ammonium sulphate calibrations were not routinely performed, so RIE$_{SO4}$ data was not available – we thus used the default RIE$_{SO4}$ of 1.2. For September 2008 (data set II) we had IE and RIE$_{NH4}$ data available, but it similarly showed a very high variability between subsequent estimates for RIE. For the 12 brute-force-single-particle (BFSP; Drewnick et al., 2015) type of calibration results available, the average ± standard deviation of RIE observed was 3.39 ± 1.20 (± 35 %; min 1.03, max 5.83). Especially for BFSP-type NH$_4$NO$_3$ calibration, uncertainty and/or bias for RIE$_{NH4}$ is high, due to low ions-per-particle (IPP) rate for NH$_4$ fragment ions, and sensitivity to threshold set for the detector (AMS best practices, Jayne, 2018).

To evaluate results for our inorganic r-CMB components, we calculated ion balance ratios for AN and AS, and compared them with theoretical values derived from compound molecular weights. The theoretical mass ratio of NH$_4$ to NO$_3$ for NH$_4$NO$_3$ is 0.29. With default RIE$_{NH4}$ of 4.0 the r-CMB AN factor yields a ratio of 0.46, and with RIE$_{NH4}$ from calibrations (3.39 ± 1.20), an average ratio of 0.54 (min 0.40, max 0.84). Results by Sun et al. (2012) produce a value of 0.36, so overall there remains discrepancy between the theoretical and observed ratios. The reason for it remains unclear, although one should note that the uncertainties involved in such estimates are generally very large if RIE uncertainty is high. The respective theoretical mass ratio for ammonium sulphate, NH$_4$: SO$_4$, is between 0.18 (NH$_4$HSO$_4$) and 0.36 ((NH$_4$)$_2$SO$_4$). Our AS r-CMB component features a ratio of 0.20 for RIE$_{NH4}$ = 4.0, and 0.24 for RIE$_{NH4}$ = 3.39. The min/max estimates due to uncertainty of RIE$_{NH4}$ (± 1.20) are (0.17…0.39). The ratio reported by Sun et al (2012) is 0.34.

As RIE is not incorporated in the factorisation phase, uncertainty in RIE does not play a role in PMF/ME-2 outcome. We did briefly test the sensitivity of the inorganic apportionment scheme to changes in RIE of NH$_4$ ion species, by running the model with RIE$_{NH4}$ ± 33% for the September 2008 data set (data set III; also presented in Section 3.2.2). The resulting model output changes are shown below, in Figure S.2 and Table S.1.

Table S.1. RIE$_{NH4}$ sensitivity test results for the inorganic apportionment scheme. ± estimate is given as ((max-min) / 2) / default result.

RIE$_{NH4}$	AS (μg/m^3)	AN (μg/m^3)	orgNO$_3$ (μg/m^3)	excess_NH$_4$ (μg/m^3)
4.00 (default)	1.562	0.139	0.105	0.032
2.68 (- 33 %)	1.473	0.031	0.202	0.003
5.32 (+ 33 %)	1.620	0.186	0.063	0.108
+/-	4.7 %	55.8 %	66.2 %	164.1 %

It thus seems the inorganic model AS component is rather insensitive to 33 % change in RIE$_{NH4}$. However, the nitrate components are much more sensitive (AN ± 56 % and orgNO$_3$ ± 66 %), and the sensitivity of "excess_NH$_4$" class to a 33 % change in RIE$_{NH4}$ is extremely high (± 164 % in mass concentrations). The changes, however, seem connected mostly to differences in scaling rather than different temporal variability, so the RIE$_{NH4}$ sensitivity does not seem to explain the difference between the inorganic ion balance scheme and the r-CMB model result. While the relative uncertainty becomes large for AN, orgNO$_3$ and excess_NH$_4$, we note this may be partly due to the generally low nitrate concentrations at SMEAR II, and the overall large uncertainty (arising from other error sources, e.g. fragmentation table calculations) in measuring low concentrations of NH$_4$ typical of the site.
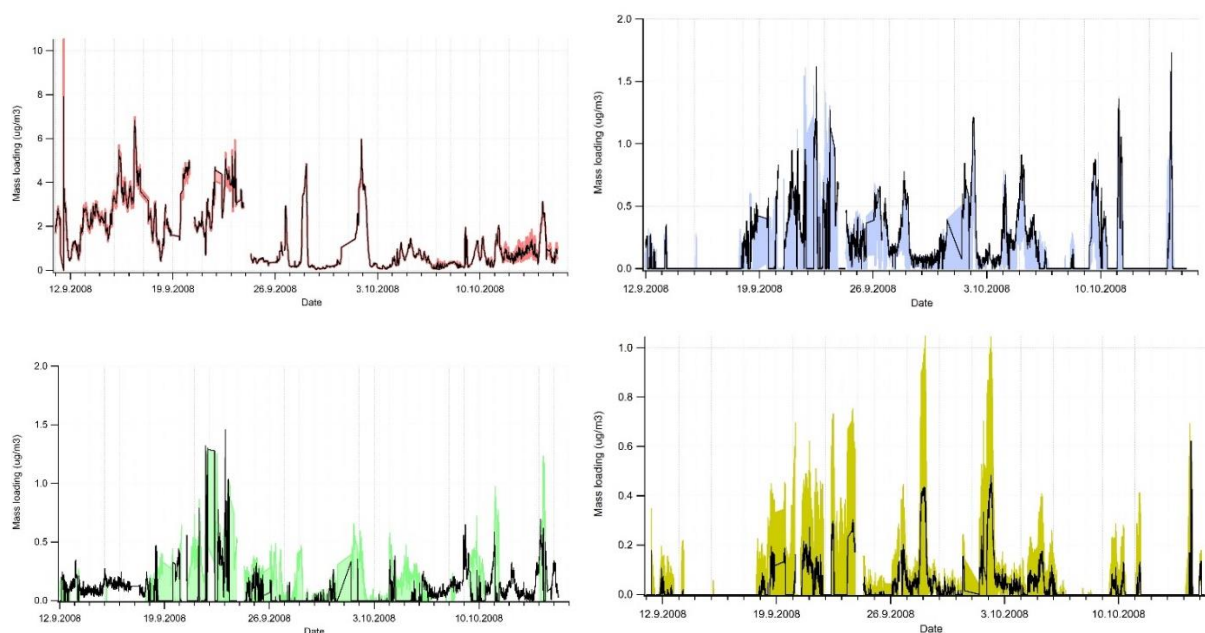
Figure S.2. RIE$_{NH4}$ sensitivity test results for the inorganic apportionment model (Sect 2.4.1), tested for data set III. Black line indicates the result with default RIE$_{NH4}$ of 4.0. Coloured areas corresponds to the min/max results for when RIE$_{NH4}$ was changed by ± 33 %. Components are colour-coded similar to main text Figure 10. (red: AS, blue: AN, green: orgNO$_3$, yellow: excess NH$_4$).

S.5 Approximation for error propagation for signal ratios

Propagation of uncertainty can be approximated by the variance formula (Ku, 1966), which yields for a ratio of two signals (s_1 and s_2) and their uncertainties (σ_1 and σ_2) an uncertainty

$$\sigma(s_1:s_2) = \sqrt{\frac{1}{s_2^2} * \sigma_1^2 + \frac{s_1^2}{s_2^4} * \sigma_2^2} \,. \tag{S.5}$$

5   In this work the above is applied in estimating the uncertainties of various signal ratios, such as σ ($NO_2^+:NO^+$).

S.6 Ammonium nitrate and ammonium sulphate calibrations and the CO_2^+ artefact
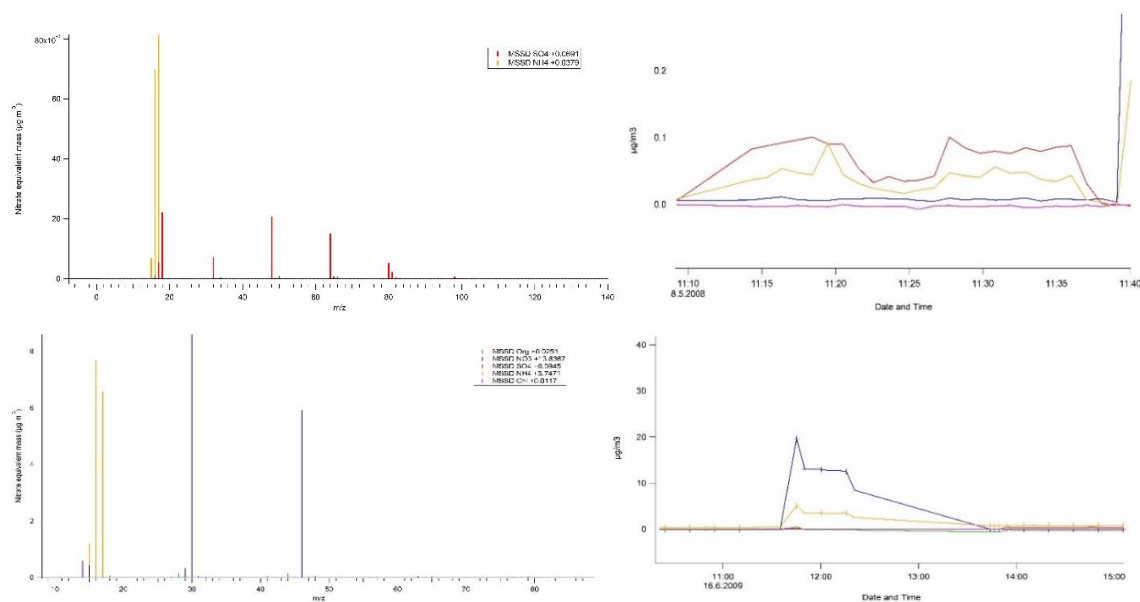
Figure S.3. AS and AN calibrations in 'MS' mode (unprocessed data). Left: mass spectra, right: time series of a calibration.

Pieber et al (2016) discuss the CO_2^+ artefact induced by thermal decomposition of inorganic salts. They find a m/z 44 Th artefact with a magnitude of 3.4% of total nitrate signal. For the phase III solution we obtain a corresponding value (for signal ratio of m/z 44 Th to NO_3) of 2.9%, suggesting most of the m/z 44 Th signal may indeed be explained by this artefact. When accounting for fragmentation-table-calculated m/z 44 Th derivatives, the same applies most of total organic signal for AN. For

15   AS (P-III), we observe a similar ratio (m/z 44 Thto SO_4) of 2.8 %, when Pieber (2016) estimate a contribution between 0.1 to 0.3 % for AS. Similar m/z 44 Th artefact is also seen for the AN calibration data (Figure S.3) above. For ON, the observed signal ratio of m/z 44 Th to NO_3 (P-III) is 22 %. Notably, the ON solution for P-I differs from the P-III solution here, with a ratio of 8.8 %. For KNO_3 Pieber et al (2016) report a ratio of 4.5 %. This also gives rise to the speculation discussed in Section 3.2.2, that the ON factor might arise from thermal decomposition of KNO_3. Furthermore, Pieber et al (2016) importantly note

that thermal decomposition of KNO_3 is temperature dependent, so vaporiser temperatures above 600 degrees Celsius would increase the observed ratio. While the standard operating temperature of the vaporiser (as per instrument readout) was used by default, oven temperature calibrations were not performed. Thus we do not have vaporiser power data available for the various campaigns to further examine the possibility of a bias in oven temperature readout, and if such a bias could connect to our observations of ON.

S.7 Phase II clustering solution

Phase II solution was obtained for $k = 15$, $s_m = 2.41$ (silh 0.6557), and is presented below.
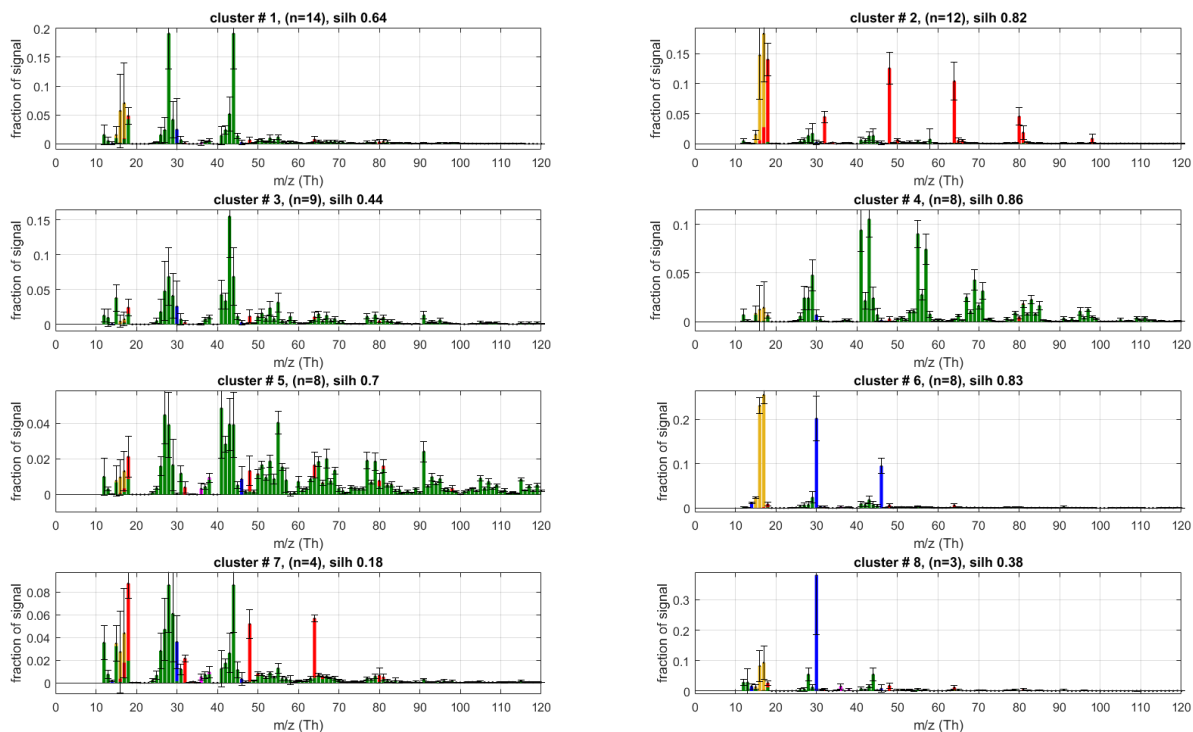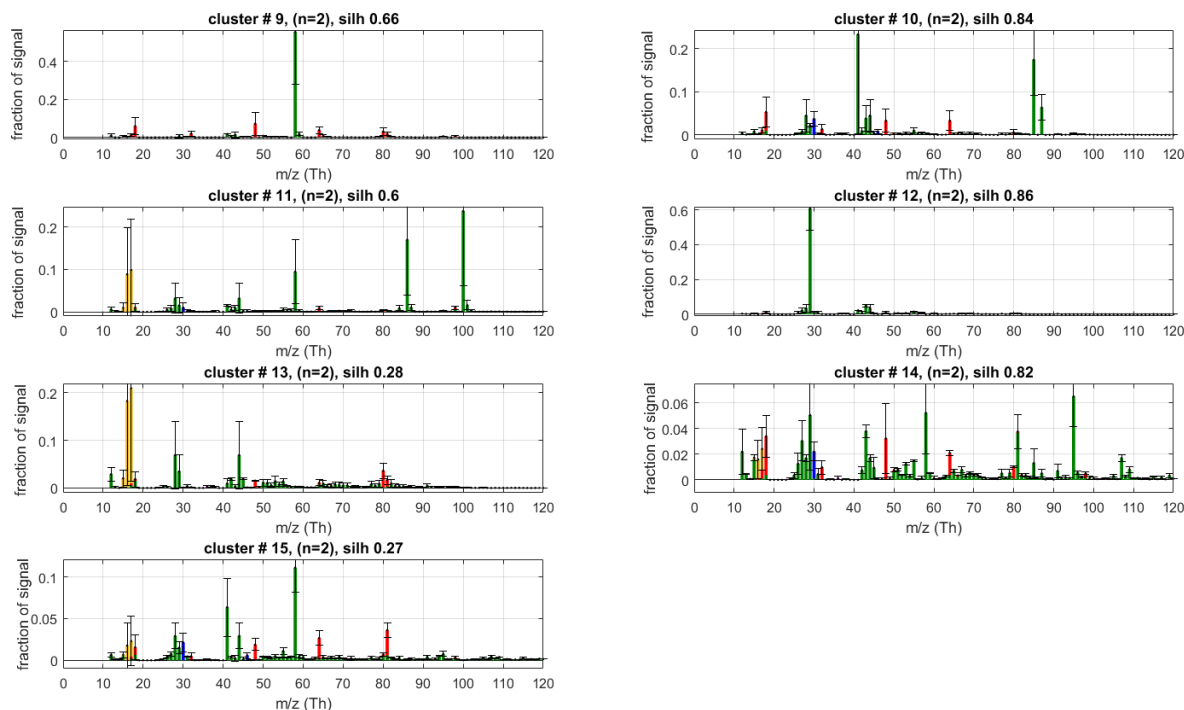
Figure S.4. P-II cluster centroids and variabilities are silhouette-weighted averages and standard deviations for the cluster members. The main SOA types were identified as cluster #1 ('low-volatile oxidised organic aerosol', LV-OOA) clusters #3 ('semi-volatile oxidised organic aerosol', SV-OOA) and cluster #7 ('organic nitrogen', ON).

S.8 CMB component inter-correlations

We calculated the mass-scaled r-CMB component profile inter-correlations to evaluate r-CMB component similarities. The result is shown in Tables S.2 (full spectrum) and S.3 (organics only). Since the scaled correlation similarity (r_s^2) also corresponds to the quantity that the clustering algorithm aims to minimise, high values for r_s are not to be expected of a robust (hard) classification solution. From the resulting similarities, it seems the distinction between AN and ON seems to be the hardest for the algorithm (with the selected metric). Also, SV-OOA shares many similar features with the LV-OOA, BBOA and HOA.

Table S.2. Squared correlation coefficients (r_s^2; $s_m = 1.81$) for CMB component spectra inter-correlations, with both organics and inorganics included. Only correlations with p-values < 0.05 are shown.

	AS	LV-OOA	SV-OOA	BBOA	ON	HOA	AN
AS	-	-	0.01	-	0.07	-	-
LV-OOA	-	-	0.43	0.07	0.23	0.07	0.01
SV-OOA	0.01	0.43	-	0.41	0.16	0.38	0.03
BBOA	-	0.07	0.41	-	0.02	0.27	-
ON	0.07	0.23	0.16	0.02	-	0.02	0.52
HOA	-	0.07	0.38	0.27	0.02	-	-
AN	-	0.01	0.03	-	0.52	-	-

Table S.3. Squared correlation coefficients (r_s^2; $s_m = 1.81$) for CMB component spectra inter-correlations, for organics only. Only correlations with p-values < 0.05 are shown.

	AS	LV-OOA	SV-OOA	BBOA	ON	HOA	AN
AS	-	0.57	0.69	0.17	0.61	0.22	0.62
LV-OOA	0.57	-	0.39	-	0.90	0.04	0.30
SV-OOA	0.69	0.39		0.34	0.51	0.31	0.77
BBOA	0.17	-	0.34	-	0.09	0.18	0.26
ON	0.61	0.90	0.51	0.09		0.09	0.43
HOA	0.22	0.04	0.31	0.18	0.09	-	0.29
AN	0.62	0.30	0.77	0.26	0.43	0.29	-

Table S.3. Pearson correlation coefficients for CMB component time series inter-correlations. Only correlations with p-values < 0.05 are shown.

	AS	LV-OOA	SV-OOA	BBOA	ON	AN	HOA
AS	-	0.21	0.00	0.25	0.21	0.16	0.07
LV-OOA	0.21	-	0.24	0.02	0.09	0.10	0.22
SV-OOA	0.00	0.24	-	0.00	0.00	0.01	0.11
BBOA	0.25	0.02	0.00	-	0.48	0.25	0.09
ON	0.21	0.09	0.00	0.48	-	0.28	0.10
AN	0.16	0.10	0.01	0.25	0.28	-	0.08
HOA	0.07	0.22	0.11	0.09	0.10	0.08	-

S.9 Mass attribution by campaign
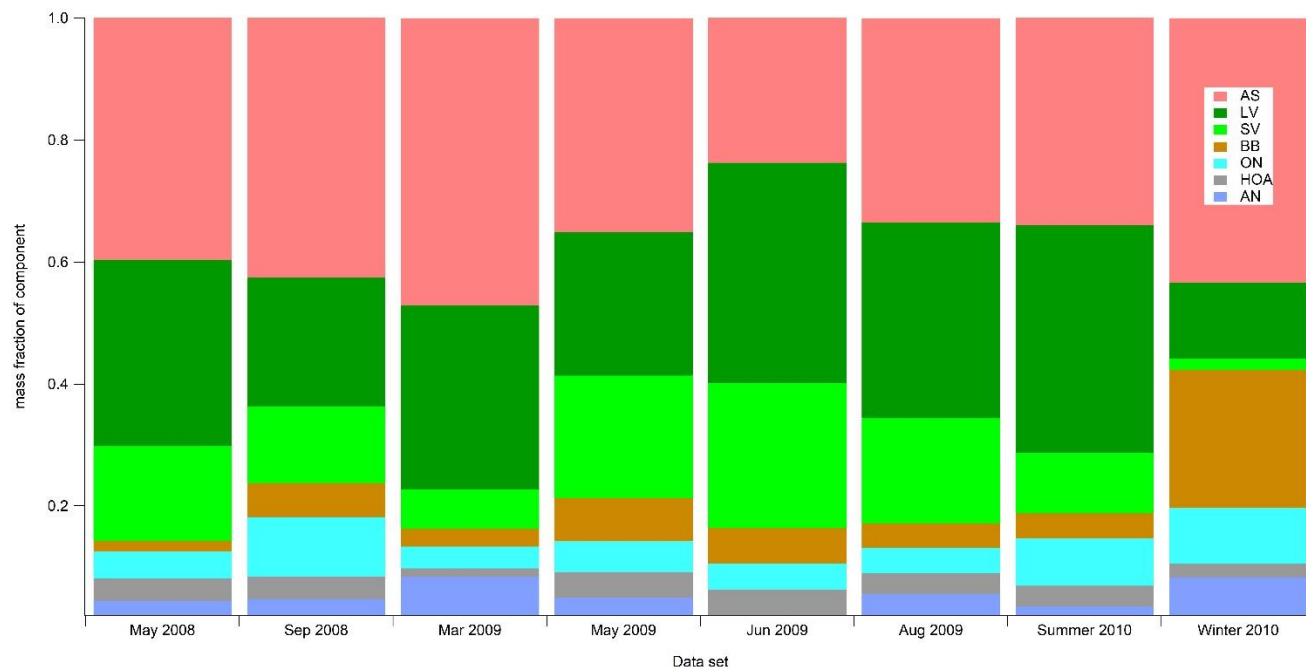
Figure S.5. Mass fractions of r-CMB component by data set. Data set VIII (Winter 2010) results are less reliable due to pronounced surface ionisation effects.

5   As discussed in 3.2.1, we consider results for data set VIII less reliable due to effects very likely stemming from pronounced surface ionisation processes. The high uncertainty is also reflected in phase I (PMF) high object function values ($Q/Q_{expected}$; see Paatero et al., 2014). The (P-I) Q/Q_{exp} diagnostic value, optimally approaching unity, was 15.29 for data set VIII, while for the other 7 data sets the mean ± standard deviation of Q/Q_{exp} was 1.32 ± 0.53, indicating the PMF model performance was good for data sets I to VII, but poor for set VIII. While a high object function value alone does not disqualify a result, it does

10 indicate the uncertainties in data were likely underestimated (e.g. Norris et al., 2008), and the model does not capture the uncertainty-weighted data variation properly, even with 10 unconstrained factors.

S.10 Cluster projections for Phase I (unconstrained PMF) result
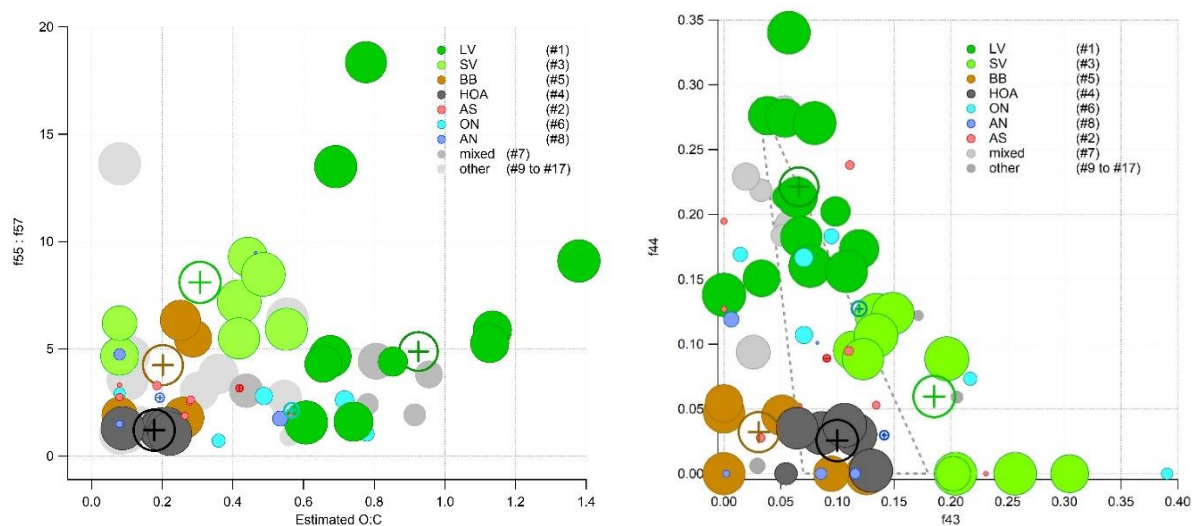
Figure S.6. (left panel) P-I solution - cluster projections onto a *f55/f57* (Mohr et al., 2012), *O:C* (estimated, Aiken et al., 2008) plane. Circles correspond to the members of the cluster and the cross markers to cluster centroids. Marker size indicates organic mass fraction in spectra. Axes are truncated. (right panel) P-I solution, projected onto *f44, f43* plane (i.e. the 'Sally's triangle' plot; Ng et al, 2010). Circles correspond to objects in cluster and the cross markers to cluster centroids. Marker size indicates organic mass fraction in spectra. Dotted line marks the area where most laboratory data for organic aerosol falls (Ng et al., 2010).

S.11 Potassium signal and surface ionisation effects
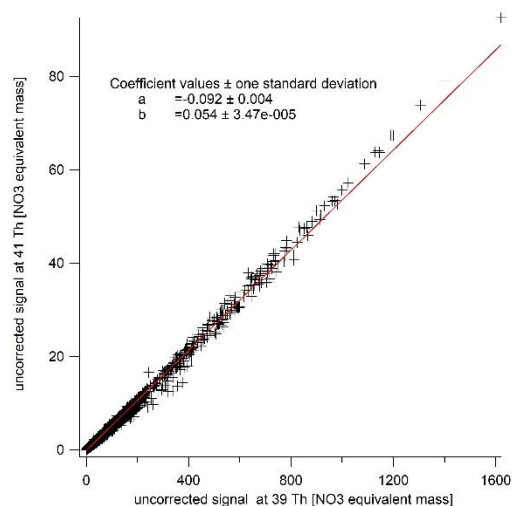
Figure S.7. X-axis: measured signal at m/z 39 Th (mainly K-39). Y-axis: measured signal at m/z 41 Th. Data is for Winter 2010 campaign (data set VIII), and contains the highest K-39 signals observed. Although corrected for in fragmentation table, the K-41 isotope correction does not fully negate the effect of potassium signal on m/z 41, which may partly explain the high m/z 41 Th signal observed affecting e.g. the BBOA component in data set VIII.
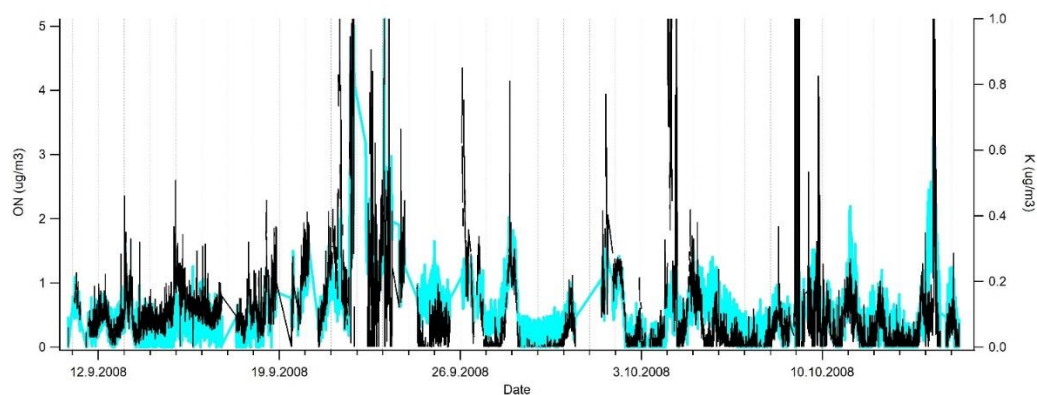
Figure S.8. On left axis: orgNO3 mass estimate from the Kiendler-Scharr parameterisation (Eq. 7) in turquoise. On the right axis: total Potassium signal in black. Although the similar temporal behaviour is at least to some extent explained by total aerosol loading, it does raise the question if surface ionisation effects could contribute to the ON component, e.g. in form of KNO_3 signal.

5 **S.12 WD analysis for Rb-containing outlier factor**
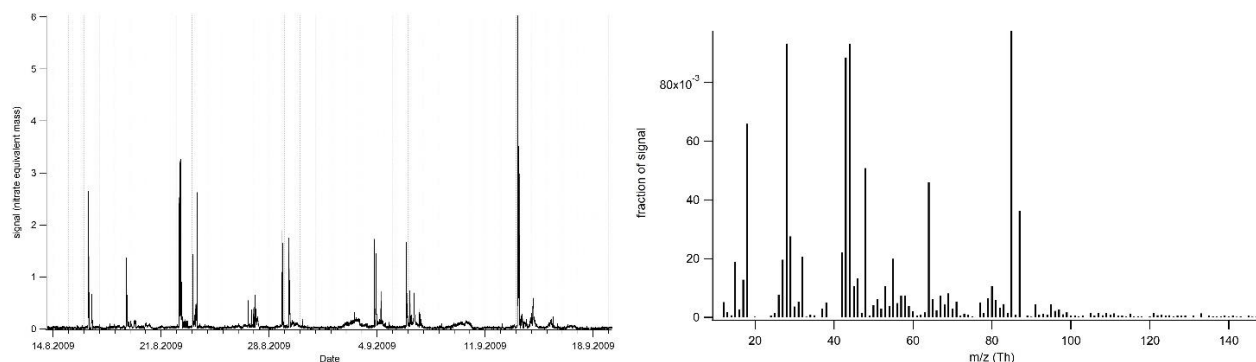
Figure S.9. Time series (left; P-I) and mass spectrum (right, P-I)) of a Rb-containing factor from data set VI.
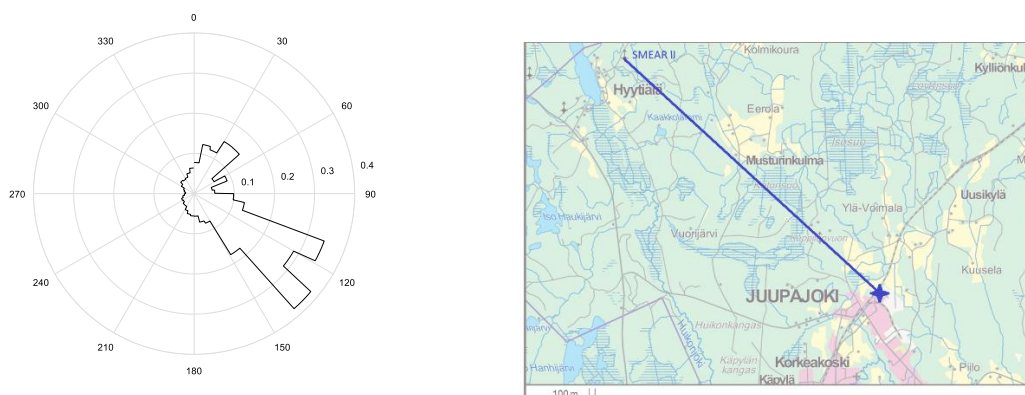
10 **Figure S.10.** Left: wind rose for the Rb containing factor from data set VI (P-I) average signal for the Rb-containing factor for wind sectors. Right: map showing the locations for SMEAR II and the Juupajoki district heating plant, co-located with a sawmill.

References

Jayne J.: AMS best practices, AMS user's meeting presentation, 2018. Available online at http://cires1.colorado.edu/jimenez-group/UsrMtgs/UsersMtg19/Jayne_CalibrationOverview.pdf, viewed 19.Sep.2018.

Aiken, A. C., Decarlo, P. F., Kroll, J. H., Worsnop, D. R., Huffman, J. A., Docherty, K. S., Ulbrich, I. M., Mohr, C., Kimmel, J. R.,
5   Sueper, D., Sun, Y., Zhang, Q., Trimborn, A., Northway, M., Ziemann, P. J., Canagaratna, M. R., Onasch, T. B., Alfarra, M. R., Prevot, A. S., Dommen, J., Duplissy, J., Metzger, A., Baltensperger, U., and Jimenez, J. L.: O/C and OM/OC ratios of primary, secondary, and ambient organic aerosols with high-resolution time-of-flight aerosol mass spectrometry, Environ Sci Technol, 42, 4478-4485, 2008.

Allan, J. D., Jimenez, J. L., Williams, P. I., Alfarra, M. R., Bower, K. N., Jayne, J. T., Coe, H., and Worsnop, D. R.: Quantitative sampling using an Aerodyne aerosol mass spectrometer 1. Techniques of data interpretation and error analysis, Journal of Geophysical Research:
10 Atmospheres (1984–2012), 108, 2003.

Buajarern, J., Mitchem, L., and Reid, J. P.: Characterizing the formation of organic layers on the surface of inorganic/aqueous aerosols by Raman spectroscopy, The Journal of Physical Chemistry A, 111, 11852-11859, 2007.

Drewnick, F., Diesch, J.-M., Faber, P., and Borrmann, S.: Aerosol mass spectrometry: particle–vaporizer interactions and their consequences for the measurements, Atmospheric Measurement Techniques, 8, 3811-3830, 2015.

15 Friedlander, S. K.: Chemical element balances and identification of air pollution sources, Environmental Science & Technology, 7, 235-240, 1973.

Gordon, G. E.: Receptor models, Environmental Science & Technology, 22, 1132-1142, 1988.

Gysel, M., Crosier, J., Topping, D., Whitehead, J., Bower, K., Cubison, M., Williams, P., Flynn, M., McFiggans, G., and Coe, H.: Closure study between chemical composition and hygroscopic growth of aerosol particles during TORCH2, Atmospheric Chemistry and Physics,
20 7, 6131-6144, 2007.

Hong, J., Äijälä, M., Häme, S. A., Hao, L., Duplissy, J., Heikkinen, L. M., Nie, W., Mikkilä, J., Kulmala, M., and Prisle, N. L.: Estimates of the organic aerosol volatility in a boreal forest using two independent methods, Atmospheric Chemistry and Physics, 17, 4387-4399, 2017.

Hopke, P. K.: Receptor modeling for air quality management, Elsevier, 1991a.

25 Hopke, P. K.: An introduction to receptor modeling, Chemometrics and Intelligent Laboratory Systems, 10, 21-43, 1991b.

Jimenez, J. L., Jayne, J. T., Shi, Q., Kolb, C. E., Worsnop, D. R., Yourshaw, I., Seinfeld, J. H., Flagan, R. C., Zhang, X. F., Smith, K. A., Morris, J. W., and Davidovits, P.: Ambient aerosol sampling using the Aerodyne Aerosol Mass Spectrometer, Journal of Geophysical Research-Atmospheres, 108, Artn 8425

10.1029/2001jd001213, 2003.

30 Kiendler-Scharr, A., Mensah, A. A., Friese, E., Topping, D., Nemitz, E., Prevot, A., Äijälä, M., Allan, J., Canonaco, F., and Canagaratna, M.: Ubiquity of organic nitrates from nighttime chemistry in the European submicron aerosol, Geophysical Research Letters, 43, 7735-7744, 2016.

Ku, H. H.: Notes on the use of propagation of error formulas, Journal of Research of the National Bureau of Standards, 70, 1966.

Miller, M., Friedlander, S., and Hidy, G.: A chemical element balance for the Pasadena aerosol, in: Aerosols and atmospheric chemistry,
35 Elsevier, 301-312, 1972.

Mohr, C., DeCarlo, P. F., Heringa, M. F., Chirico, R., Slowik, J. G., Richter, R., Reche, C., Alastuey, A., Querol, X., Seco, R., Penuelas, J., Jimenez, J. L., Crippa, M., Zimmermann, R., Baltensperger, U., and Prevot, A. S. H.: Identification and quantification of organic aerosol from cooking and other sources in Barcelona using aerosol mass spectrometer data, Atmospheric Chemistry and Physics, 12, 1649-1665, 10.5194/acp-12-1649-2012, 2012.

40 Ng, N. L., Canagaratna, M. R., Zhang, Q., Jimenez, J. L., Tian, J., Ulbrich, I. M., Kroll, J. H., Docherty, K. S., Chhabra, P. S., Bahreini, R., Murphy, S. M., Seinfeld, J. H., Hildebrandt, L., Donahue, N. M., DeCarlo, P. F., Lanz, V. A., Prevot, A. S. H., Dinar, E., Rudich, Y., and Worsnop, D. R.: Organic aerosol components observed in Northern Hemispheric datasets from Aerosol Mass Spectrometry, Atmospheric Chemistry and Physics, 10, 4625-4641, 10.5194/acp-10-4625-2010, 2010.

Norris, G., Vedantham, R., Wade, K., Brown, S., Prouty, J., and Foley, C.: EPA positive matrix factorization (PMF) 3.0 fundamentals &
45 user guide, Prepared for the US Environmental Protection Agency, Washington, DC, by the National Exposure Research Laboratory, Research Triangle Park, 2008.

Paatero, P., Eberly, S., Brown, S. G., and Norris, G. A.: Methods for estimating uncertainty in factor analytic solutions, Atmospheric Measurement Techniques, 7, 781-797, 10.5194/amt-7-781-2014, 2014.

Pieber, S. M., El Haddad, I., Slowik, J. G., Canagaratna, M. R., Jayne, J. T., Platt, S. M., Bozzetti, C., Daellenbach, K. R., Fröhlich, R.,
50 and Vlachou, A.: Inorganic salt interference on CO2+ in aerodyne AMS and ACSM organic aerosol composition studies, Environmental science & technology, 50, 10494-10503, 2016.

Sun, Y., Zhang, Q., Schwab, J., Yang, T., Ng, N., and Demerjian, K.: Factor analysis of combined organic and inorganic aerosol mass spectra from high resolution aerosol mass spectrometer measurements, Atmospheric Chemistry and Physics, 12, 8537-8551, 2012.